

Systematic study of optical potential strengths in reactions on ^{120}Sn involving strongly bound, weakly bound, and exotic nuclei

M. A. G. Alvarez , J. P. Fernández-García , and J. L. León-García
Departamento FAMN, Universidad de Sevilla, Apartado 1065, 41080 Sevilla, Spain

M. Rodríguez-Gallardo
Departamento FAMN, Universidad de Sevilla, Apartado 1065, 41080 Sevilla, Spain
and Instituto Carlos I de Física Teórica y Computacional, Universidad de Sevilla, Spain

L. R. Gasques , L. C. Chamon , V. A. B. Zagatto, A. Lépine-Szilý, and J. R. B. Oliveira 
Universidade de Sao Paulo, Instituto de Física, Rua do Matao, 1371, 05508-090 Sao Paulo, SP, Brazil

V. Scarduelli
Instituto de Física, Universidade Federal Fluminense, 24210-340 Niterói, Rio de Janeiro, Brazil
and Instituto de Física da Universidade de São Paulo, 05508-090 São Paulo, SP, Brazil

B. V. Carlson
Departamento de Física, Instituto Tecnológico de Aeronáutica, São José dos Campos, SP, Brazil

J. Casal
Dipartimento di Fisica e Astronomia “G. Galilei” and INFN-Sezione di Padova, Via Marzolo, 8, I-35131 Padova, Italy

A. Arazi
Laboratorio TANDAR, Comisión Nacional de Energía Atómica, Av. Gral. Paz 1499, BKNA1650 San Martín, Argentina

D. A. Torres  and F. Ramirez 
Departamento de Física, Universidad Nacional de Colombia, Bogotá, Colombia



(Received 26 July 2019; published 5 December 2019)

We present new experimental angular distributions for the elastic scattering of $^6\text{Li} + ^{120}\text{Sn}$ at three bombarding energies. We include these data in a wide systematic involving the elastic scattering of $^4,^6\text{He}$, ^7Li , ^9Be , ^{10}B , and $^{16,18}\text{O}$ projectiles on the same target at energies around the respective Coulomb barriers. Considering this data set, we report on optical model analyses based on the double-folding São Paulo potential. Within this approach, we study the sensitivity of the data fit to different models for the nuclear matter densities and to variations in the optical potential strengths.

DOI: [10.1103/PhysRevC.100.064602](https://doi.org/10.1103/PhysRevC.100.064602)

I. INTRODUCTION

Nuclei present cluster structures [1]. Light, strongly, or weakly bound, stable or exotic, nuclei such as ^6He , $^6,^7\text{Li}$, $^{7,8,9}\text{Be}$, $^{12,13,14}\text{C}$, $^{16,18}\text{O}$, among others (isotopes and nuclei), can be considered as results of n , $^1,^2,^3\text{H}$, and $^3,^4\text{He}$ combinations. This has been evidenced by experimental observations on breakup or transfer reactions (e.g., Refs. [2–5]). The ^4He possesses a significantly higher binding energy per nucleon than its light neighbors (see Table I), and a first excited state with very high excitation energy (20.6 MeV) that makes it a rather robust and inert nucleus.

Unlike ^4He , ^6He is an exotic nucleus that decays, by beta minus emission, in ^6Li , with a half-life of 806.7(15) ms [6]. It is a Borromean nucleus, i.e., the two subsystems, $^4\text{He}-n$ and $n-n$, are not bound. Reactions induced by ^6He on different

targets, at energies around the Coulomb barrier, exhibit a remarkable large cross section for α particles production [3,4]. This confirms a breakup picture, which is associated to the weak binding of the halo neutrons ($S_{2n} = 0.98$ MeV, Table I) [6], that favors the dissociation of the ^6He projectile.

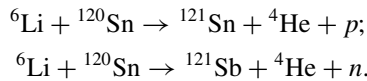
^7Li is one of the heaviest nuclides formed with very small yields during the primordial Big Bang nucleosynthesis. Stable nuclei heavier than ^7Li were formed much later through light nuclei reacting during stellar evolution or explosions. Despite small amounts of ^6Li and ^7Li being produced in stars, they are expected to be burned very fast. Additional small amounts of both ^6Li and ^7Li may be generated from cosmic ray spallation on heavier atoms in the interstellar medium, from solar wind and from early solar system ^7Be and ^{10}Be radioactive decays [7].

TABLE I. Binding energy per nucleon, proton, and neutron separation energies, possible mode of breakup and corresponding Q value for some nuclei. All energies are provided in MeV.

Nucleus	BE/A	S_{1p}	S_{1n}	Cluster	Q
^4He	7.07	19.81	20.58		
^6He	4.88	22.59	1.71	$\alpha + n + n$	-0.98
^6Li	5.33	4.43	5.66	$\alpha + d$	-1.47
^7Li	5.61	9.97	7.25	$\alpha + t$	-2.47
^9Be	6.46	16.89	1.66	$\alpha + \alpha + n$	-1.57
^{10}B	6.47	6.59	8.44	$^6\text{Li} + \alpha$	-4.46
^{11}B	6.93	11.23	11.54	$^7\text{Li} + \alpha$	-8.66

Both ^6Li and ^7Li have an anomalous low nuclear binding energy per nucleon compared to their stable neighbors (see Table I). In fact, these lithium isotopes have lower binding energy per nucleon than any other stable nuclide with $Z > 3$. As a consequence, even being light, $^6,7\text{Li}$ are less common in the solar system than 25 of the first 32 chemical elements [8]. The ^6Li and ^7Li nuclei are stable weakly bound isotopes for which strong breakup effects are expected in collisions with other nuclei. These isotopes can be considered as $\alpha + d$ and $\alpha + t$ clusters, with small Q values (see Table I).

Luong *et al.* [2] showed that breakup of ^6Li into its $\alpha + d$ constituents dominates in reactions with heavy targets. However, breakup triggered by nucleon transfer is highly probable. As an example, in the case of a ^6Li beam focusing on a ^{120}Sn target these processes could be:



These strong breakup mechanisms triggered by nucleon transfer help in explaining the large number of α particles observed in different ^6Li reactions [2,9]. In Table II, we present Q values of possible breakup processes triggered by transfer for systems involving some weakly bound projectiles on a ^{120}Sn target.

Unlike ^6Li , ^7Li presents a first excited state with relatively low excitation energy ($E^* = 0.48$ MeV). The ^7Li nucleus also has a small binding energy for the $\alpha + t$ breakup, which is, however, about 1 MeV higher than that for ^6Li (see Table I). Even so, in reactions of ^7Li , the breakup channel of the $\alpha + t$ cluster is relevant [2]. Notwithstanding, ^8Be formation (with

TABLE II. Q values of some breakup processes triggered (or not) by transfer for weakly bound projectiles colliding with a ^{120}Sn target.

Projectile	Reaction products	$Q(\text{MeV})$
^6Li	$^{121}\text{Sn} + \alpha + p$	2.472
^6Li	$^{121}\text{Sb} + \alpha + n$	2.092
^7Li	$^{122}\text{Sn} + \alpha + p$	4.036
^7Li	$^{122}\text{Sb} + \alpha + n$	1.247
^9Be	$^{121}\text{Sn} + \alpha + \alpha$	4.597
^9Be	$^{120}\text{Sn} + ^8\text{Be} + n$	4.505
^{10}B	$^{121}\text{Sn} + 2\alpha + p$	-1.989
^{10}B	$^{121}\text{Sb} + 2\alpha + n$	-2.368

subsequent $\alpha + \alpha$ decay) through a proton pick-up transfer process ($Q = 6.658$ MeV) is more probable.

The ^9Be nucleus presents a Borromean structure composed of two α particles and one weakly bound neutron [10]. It has a binding energy for the $\alpha + \alpha + n$ breakup comparable to that for ^6Li (see Table I). The $1n$ -separation energy of ^9Be is quite small in comparison with those for the other nuclei of Table I. Thus, when colliding with a target nucleus, ^9Be tends (with high probability) to transfer its weakly bound neutron, with $\alpha + \alpha$ or ^8Be formation (the later followed by $\alpha + \alpha$ decay). In Ref. [11], Arazi *et al.* demonstrated the importance of couplings to unbound states to obtain theoretical agreement with the $^9\text{Be} + ^{120}\text{Sn}$ data set, at energies around the Coulomb barrier, corroborating breakup as an important process.

Similar to ^7Li , ^{10}B also presents a first excited state with low excitation energy ($E^* = 0.72$ MeV). However, compared to $^6,7\text{Li}$ and ^9Be (Table I), its most favorable breakup channel, $^{10}\text{B} \rightarrow ^6\text{Li} + ^4\text{He}$, is energetically higher and, therefore, less probable. In addition, considering the different values of the $1n$ -separation energy (Table I), breakup triggered by nucleon transfer is not as favored for ^{10}B as it is for ^9Be . In Ref. [12], we demonstrated that couplings to the continuum states are not important to obtain a good agreement between theoretical calculations and experimental data for $^{10}\text{B} + ^{120}\text{Sn}$, at energies around the Coulomb barrier, indicating that breakup is not an important process in this case. The above-mentioned features indicate a very different reaction dynamics for ^9Be and ^{10}B weakly bound projectiles reacting with ^{120}Sn .

Studying reactions involving weakly bound stable nuclei is a crucial step towards a better understanding of their abundances. The structural models of these nuclei are fundamental to determine how they interact and, therefore, to shed light on such abundances. Weakly bound nuclei, in general, have fundamental structural characteristics, such as the above mentioned low breakup thresholds and cluster structures. Breakup can lead to a complex problem of three or more bodies, and can occur by direct excitation of the weakly bound projectile into continuum states or by populating continuum states of the target [3,13–18].

Weakly bound stable nuclei can easily be produced and accelerated, with high intensities, in conventional particle accelerators. Within this context, complementary experimental campaigns are being developed in two laboratories: the 8 MV tandem accelerator of the Open Laboratory of Nuclear Physics (LAFN) in the Institute of Physics of the University of São Paulo (Brazil), and the 20 MV tandem accelerator TANDAR (Buenos Aires, Argentina). The aim of the joint collaboration is to study the scattering involving stable, strongly and weakly bound, nuclei on the same target (^{120}Sn), at energies around the respective Coulomb barriers. These measurements allow systematic studies that involve the comparison of behavior for the different projectiles.

Many data, obtained in our experiments, with ^{120}Sn as target, have already been published [11,12,19,20]. In the present paper, we present new experimental angular distributions for the elastic scattering of the $^6\text{Li} + ^{120}\text{Sn}$ system, at three bombarding energies. We include these data in a wide systematic involving the elastic scattering of $^4,6\text{He}$, ^7Li , ^9Be , ^{10}B , and $^{16,18}\text{O}$ projectiles, on the same target, at energies around the

respective Coulomb barriers. We analyze the complete data set within the approach of the optical model (OM), assuming the double-folding São Paulo potential (SPP) [21] for the real part of the optical potential (OP) and two different models for the imaginary part. With this, we study the behavior of the OP as a function of the energy for the different projectiles.

In the next section, we present a summarized review of the experiments. It will be followed by the explanation of the theoretical approach and corresponding application to the experimental data. Then, we discuss and compare the behaviors of the OPs that fit the data for different projectiles. Finally, we present our main conclusions.

II. EXPERIMENTS

The measurements for the ${}^6,7\text{Li}$, ${}^{10,11}\text{B}$ + ${}^{120}\text{Sn}$ systems are part of the E-125 experimental campaign, developed at the LAFN, and correspond to the following energies: (i) ${}^6\text{Li}$ at $E_{\text{LAB}} = 19, 24, \text{ and } 27$ MeV, reported for the first time in this paper; (ii) ${}^7\text{Li}$ at $E_{\text{LAB}} = 20, 22, 24, \text{ and } 26$ MeV [19]; (iii) ${}^{10}\text{B}$ at $E_{\text{LAB}} = 31.35, 33.35, 34.85, \text{ and } 37.35$ MeV [12,20]. The experimental setup is based on SATURN (Silicon Array based on Telescopes of USP for Reactions and Nuclear applications). SATURN is installed in the 30B experimental beam line of the laboratory, which contains a scattering chamber connected to the accelerator. The SATURN detection system has been mounted with nine surface barrier detectors in angular intervals of 5° . With this, in three runs we cover an angular range of 120° , from 40° – 160° . The targets contained ${}^{120}\text{Sn}$ and ${}^{197}\text{Au}$, the latter used for the purpose of normalization. Further details are found in Refs. [12,19,20].

The experimental data for ${}^9\text{Be}$ + ${}^{120}\text{Sn}$ were obtained at the TANDAR laboratory, at $E_{\text{LAB}} = 26, 27, 28, 29.5, 31, 42, \text{ and } 50$ MeV. An array of eight surface barrier detectors, with an angular separation of 5° between adjacent detectors, was used to distinguish scattering products. All details about data acquisition and analysis are presented in Ref. [11]. In addition to our data, other experimental elastic scattering cross sections, for systems involving ${}^{120}\text{Sn}$ as target, were obtained from Refs. [22–29].

III. THEORETICAL APPROACH

Data of heavy-ion nuclear reactions have been successfully described in many works assuming double-folding theoretical models for the nuclear potential [30–38]. Among these models, the SPP [21] associates the nuclear interaction to a dependence on the local velocity. The model includes a systematic of nuclear densities obtained for stable strongly bound nuclei and, in this context, it does not contain any free parameter. The SPP is related to the double-folding potential through:

$$V_{\text{SPP}}(R) = V_{\text{Fold}}(R) e^{-4v^2/c^2}, \quad (1)$$

where c is the speed of light and $v(R)$ is the local relative velocity between projectile and target. At energies around the Coulomb barrier (as in the present analysis) the velocity is much smaller than the speed of light and we have: $V_{\text{SPP}}(R) \approx$

$V_{\text{Fold}}(R)$. The folding potential is represented as:

$$V_{\text{Fold}}(R) = \iint \rho_1(\vec{r}_1) \rho_2(\vec{r}_2) V_0 \delta(\vec{R} - \vec{r}_1 + \vec{r}_2) d\vec{r}_1 d\vec{r}_2. \quad (2)$$

Here, ρ_1 and ρ_2 are the projectile and target matter distributions, and $V_0 \delta(\vec{r})$ is the zero-range effective interaction (with $V_0 = -456$ MeV fm³). This V_0 value was obtained in Ref. [21], through a very wide systematic involving phenomenological potentials extracted from elastic scattering data analyses for many systems. For a particular nucleus, the respective nucleon distribution is folded with the matter density of one nucleon to obtain the corresponding matter density of the nucleus (see Ref. [21]).

An important point that stands out against obtaining a systematical description of the elastic scattering process with an OP (within the OM) is the difficulty in describing the imaginary part of the interaction from fundamental grounds. A fully microscopic description based on the Feshbach theory is especially difficult at energies where collective as well as single-particle excitations are important in the scattering process [39–41]. To face this problem within a simple model, an extension of the SPP to the OP imaginary part was proposed in Ref. [42], considering the following OP:

$$U_{\text{OP}}(R) = V_{\text{SPP}}(R) + i N_I V_{\text{SPP}}(R). \quad (3)$$

Elastic scattering data for many systems, at high energies, have been described using $N_I \approx 0.78$ [42]. At energies around the Coulomb barrier, the SPP has also been valuable in coupled channel calculations for systems involving strongly (see, e.g., Ref. [43]) and weakly bound (e.g., Refs. [12,19,20]) projectiles. Furthermore, the SPP has accounted for data of systems with exotic nuclei (e.g., Refs. [44,45]). Besides being successful in elastic scattering data analyses, the SPP has also provided good descriptions of data for the fusion process of many systems (e.g., Refs. [46–50]).

In the present work, we propose the SPP theoretical approach in the context of the OM to systematically study the elastic scattering data for the ${}^4,6\text{He}$, ${}^6,7\text{Li}$, ${}^9\text{Be}$, ${}^{10}\text{B}$, ${}^{16,18}\text{O}$ + ${}^{120}\text{Sn}$ systems, at energies around the Coulomb barrier. We assume Eq. (4) to describe the OP:

$$U_{\text{OP}}(R) = N_R V_{\text{SPP}}(R) + i N_I V_{\text{SPP}}(R), \quad (4)$$

where N_R and N_I represent multiplicative factors that determine the strengths of the OP (real and imaginary parts) and simulate, in a simple form, the effects of the polarization potential. The polarization arises from nonelastic couplings. According to Feshbach's theory [38,51], it is energy dependent and complex. The imaginary part comes from transitions to open nonelastic channels that absorb flux from the elastic channel. The real part arises from virtual transitions to intermediate states (inelastic excitations, nucleon transfer, among others). As already commented, standard average values obtained in Ref. [42] are $N_R = 1$ and $N_I = 0.78$.

For the purpose of comparison and with the aim of accounting only for the internal absorption (fusion) from barrier penetration, without taking into account the effect of the couplings, we also perform OM calculations based on Eq. (5):

$$U_{\text{OP}}(R) = V_{\text{SPP}}(R) + i W(R), \quad (5)$$

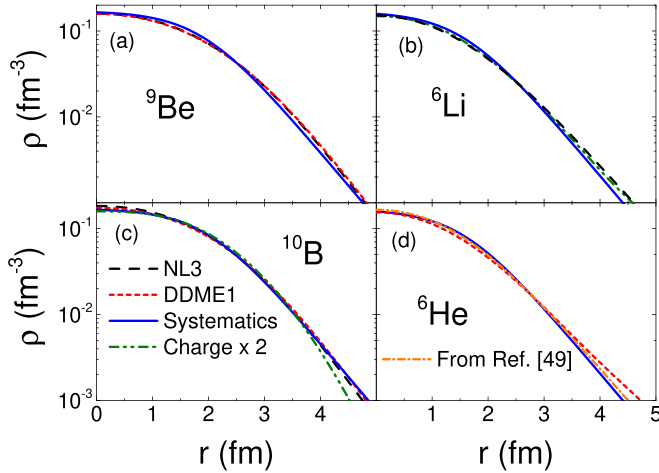


FIG. 1. Matter densities for ^{10}B , ^9Be , ^6Li , and ^6He , calculated through different models (see text for details).

where $W(R)$ has a Woods-Saxon (WS) shape,

$$W(R) = W_0/[1 + \exp(R - R_0)/a], \quad (6)$$

with $W_0 = -100$ MeV, $R_0 = r_0(A_1^{1/3} + A_2^{1/3})$, $r_0 = 1.06$ fm, and $a = 0.25$ fm. Due to the small diffuseness value, such an internal imaginary potential just simulates the fusion process (without couplings) and does not take into account the absorption by the peripheral channels.

Before proceeding with the OM analyses, we first examine the effects of the densities on the nuclear interaction. As already commented, the SPP involves a systematics of densities that makes the interaction a parameter-free model. However, one can question if the use of this systematics for weakly bound nuclei is appropriate. Thus, we have calculated nuclear densities through theoretical Hartree-Bogoliubov (HB) calculations [52], assuming two different interactions: the NL3 and DDME1 models [53,54]. Figure 1 shows a comparison of different approaches for the matter densities of light weakly bound nuclei: the two-parameter Fermi systematics of the SPP and the theoretical HB. In the cases of ^6Li and ^{10}B (where $N = Z$), we also present in Fig. 1 the experimental charge density (obtained from electron scattering) multiplied by 2. Except for ^6He , all these densities are very similar, and therefore the use of the systematics for densities of the SPP is justified. We have also verified that very similar values of cross sections are obtained from OM calculations using these different models for the densities. In the ^6He case, the theoretical HB density is rather different from that of the systematics at the surface region. Thus, we have taken an experimental density for this nucleus, obtained from data analyses of proton scattering at high energies [55]. The dashed-dotted orange line in Fig. 1(d) represents this experimental matter density (obtained from folding the nucleon distribution with the matter density of the nucleon, according to Ref. [21]). The experimental density is quite similar to that from the systematics of the SPP (blue line). Thus we consider that, even in the ^6He case, the use of the SPP systematics for densities is justified.

TABLE III. Values of the s -wave barrier parameters obtained with the SPP for systems composed by projectiles focusing on ^{120}Sn .

projectile	V_B (MeV)	R_B (fm)	$\hbar\omega$ (MeV)
^4He	14.22	9.48	4.92
^6He	12.78	10.52	3.35
^6Li	19.76	10.16	4.20
^7Li	19.45	10.34	3.86
^9Be	25.78	10.40	3.93
^{10}B	32.38	10.34	4.17
^{16}O	50.79	10.56	4.14
^{18}O	50.05	10.74	3.86

IV. STANDARD OPTICAL MODEL CALCULATIONS

Before providing the results of the elastic scattering data fits, we present a comparison of the experimental angular distributions with OM cross sections obtained assuming the standard models for the OP. By standard models we mean Eq. (4) with $N_R = 1$ and $N_I = 0.78$, and Eq. (5) (internal imaginary potential). From now on, we refer to these standard models as strong surface absorption (SSA) and only internal absorption (OIA), respectively. In order to illustrate the region of energy of the data, for each angular distribution we provide the value of the reduced energy, defined as:

$$E_{\text{Red}} = E_{\text{c.m.}} - V_B, \quad (7)$$

where $E_{\text{c.m.}}$ represents the center of mass energy and V_B is the s -wave barrier height, obtained for the respective system with the SPP. In Table III we present the barrier heights, radii, and curvatures ($\hbar\omega$) [46], for the systems studied in the present work.

Figure 2 presents four experimental angular distributions for the strongly bound ^4He projectile [22]. The energies

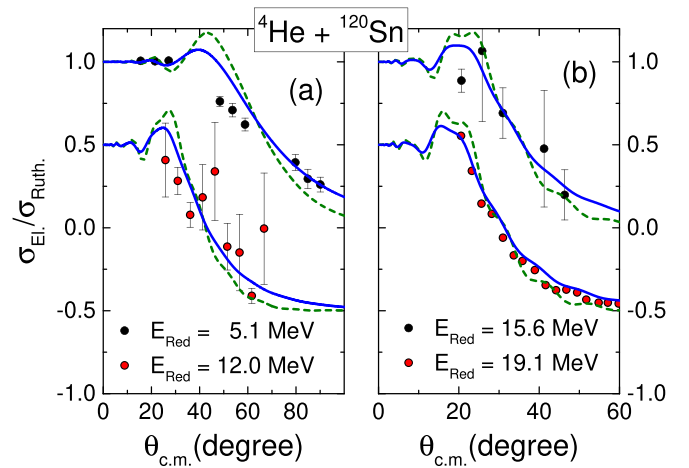


FIG. 2. Experimental angular distributions for the elastic scattering of the $^4\text{He} + ^{120}\text{Sn}$ system [22,23]. To avoid overlapping results, the cross sections for $E_{\text{Red}} = 12.0$ and 19.1 MeV have been displaced by a constant factor of 0.5. The solid and dashed lines represent theoretical OM cross sections obtained with the SSA and OIA models, respectively.

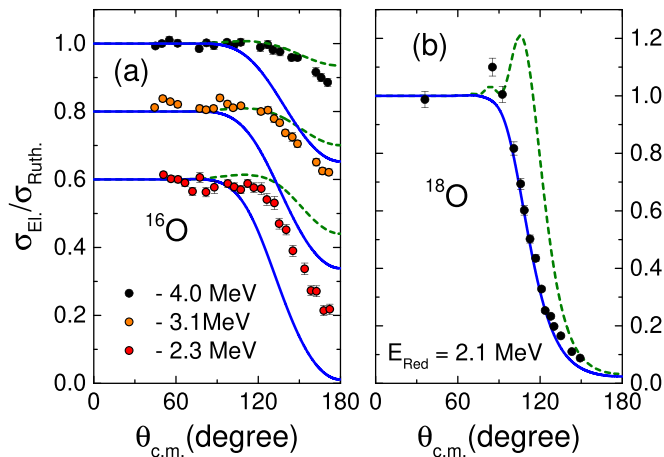


FIG. 3. Experimental angular distributions for the $^{16,18}\text{O} + ^{120}\text{Sn}$ systems [24,25]. To avoid overlapping results, the cross sections for some distributions have been displaced by a constant factor. The solid and dashed lines represent theoretical OM cross sections obtained with the SSA (solid) and OIA (dashed) models, respectively

of the angular distributions vary from 5.1–19.1 MeV above the barrier ($5.1 \leq E_{\text{Red}} \leq 19.1$ MeV). To avoid overlapping results, the cross sections for two angular distributions have been displaced by a constant factor of 0.5. The solid blue and dashed green lines represent the theoretical results obtained with SSA and OIA, respectively. Both standard models provide rather similar results, but the SSA accounts for the data with slightly better accuracy.

Figure 3 presents experimental and theoretical (SSA and OIA) angular distributions for the strongly bound ^{16}O and ^{18}O projectiles. In the ^{16}O case, all energies are below the corresponding barrier height. At the lowest energy ($E_{\text{Red}} = -4.0$ MeV) the data are compatible with internal absorption (OIA), while for higher energies they approach to the results of strong surface absorption (SSA). In the case of ^{18}O , the energy is slightly above the barrier and the SSA reproduces well the data set, except at the rainbow region ($\theta_{\text{c.m.}} \approx 90^\circ$).

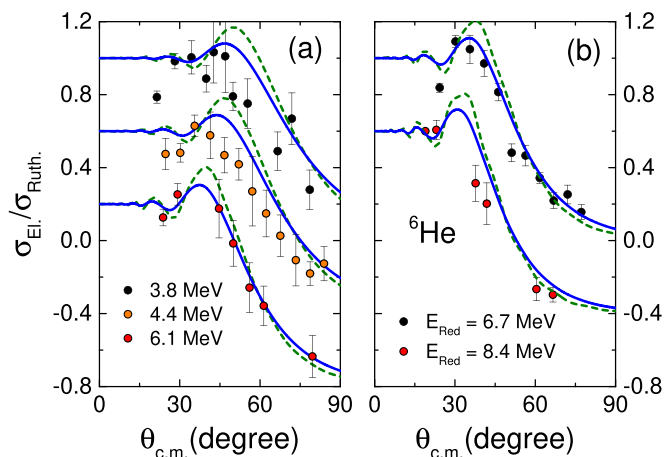


FIG. 4. The same as Fig. 3, for the $^6\text{He} + ^{120}\text{Sn}$ system. Data were extracted from Refs. [26,27].

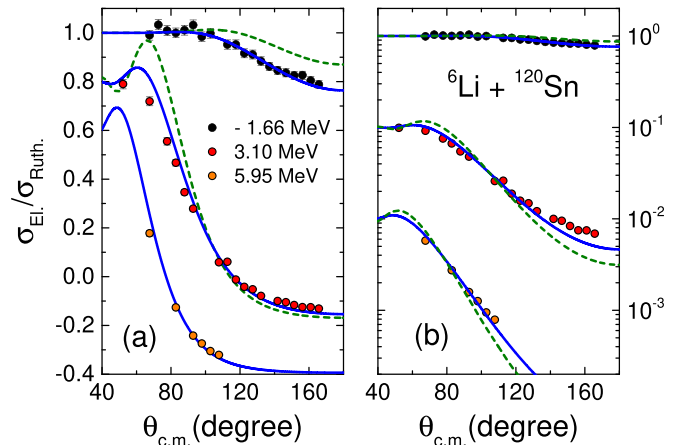


FIG. 5. Experimental and theoretical SSA (solid lines) and OIA (dashed lines) elastic scattering angular distributions for $^6\text{Li} + ^{120}\text{Sn}$. Note the change from linear (a) to logarithmic (b) scale. To avoid superposition, the cross sections for two distributions are displaced (a) or divided (b) by constant factors.

Figure 4 presents data and theoretical predictions (SSA and OIA) for the elastic scattering of the exotic ^6He on ^{120}Sn [26,27]. Again the SSA provides a good description of the data, with some deviation for the lowest $E_{\text{Red}} = 3.8$ and 4.4 MeV, due to transfer/breakup channels [27].

In Fig. 5, with the present new data, we show theoretical predictions for $^6\text{Li} + ^{120}\text{Sn}$, at energies around the barrier, in linear [Fig. 5(a)] and logarithmic [Fig. 5(b)] scales. The SSA cross sections (solid blue lines) are in good agreement with the data, including at $E_{\text{Red}} = -1.66$ MeV, which indicates strong surface absorption even in the sub-barrier energy region. For comparison, in Fig. 6 we present an excitation function for the elastic scattering of $^6\text{Li} + ^{120}\text{Sn}$ from earlier measurements [28]. The data correspond to an angular range of $160^\circ \leq \theta_{\text{Lab}} \leq 170^\circ$. The solid line represents the SSA cross sections at the average angle $\theta_{\text{c.m.}} = 165.7^\circ$. There is a reasonable agreement between experimental and theoretical results, but

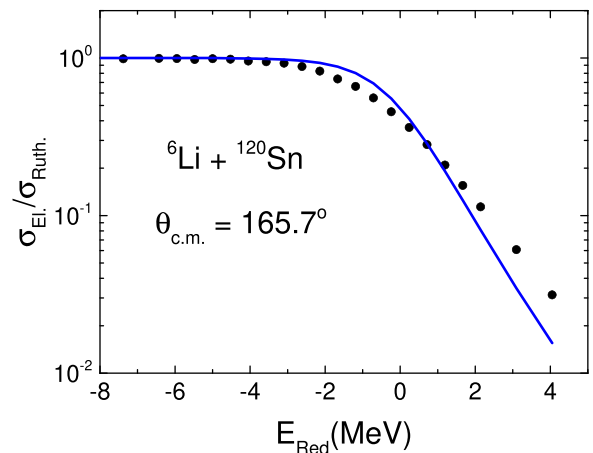


FIG. 6. Experimental excitation function for $^6\text{Li} + ^{120}\text{Sn}$ [28] (see text for details). The solid line represents the SSA cross sections at $\theta_{\text{c.m.}} = 165.7^\circ$.

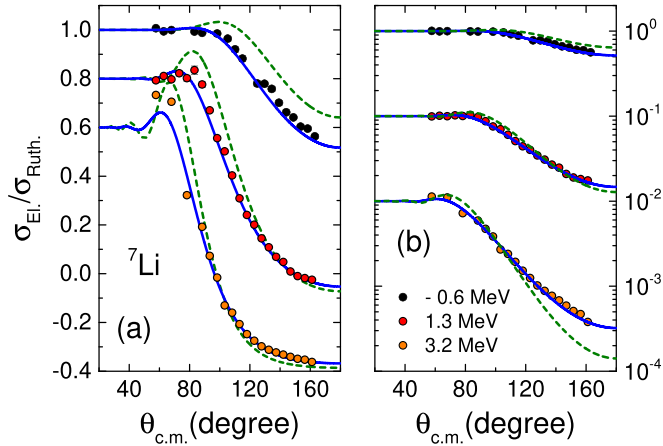


FIG. 7. The same as Fig. 5, for $^7\text{Li} + ^{120}\text{Sn}$. Data were extracted from Ref. [19].

the slope of the data is somewhat different from that of the OM calculations.

Figures 7 and 8 present results for $^7\text{Li} + ^{120}\text{Sn}$ [19]. In this case, the SSA provides even better agreement between data and theory than for ^6Li .

Figures 9 and 10 present results for $^9\text{Be} + ^{120}\text{Sn}$. Again, the SSA provides cross sections in reasonable agreement with the data.

Finally, Fig. 11 presents results for $^{10}\text{B} + ^{120}\text{Sn}$. The SSA does not work as well as in other cases of weakly bound nuclei. However, the reduced energy region in the case of ^{10}B is low and the results for this nucleus are similar to those shown for ^{16}O in Fig. 3(a).

V. COMPARISON OF THE BEHAVIOR OF THE OPTICAL POTENTIAL FOR DIFFERENT PROJECTILES

As commented in the previous section, the SSA provides an overall reasonable description of the complete data set studied here. Even so, small deviations between data and theoretical predictions are observed. In this section, we assume

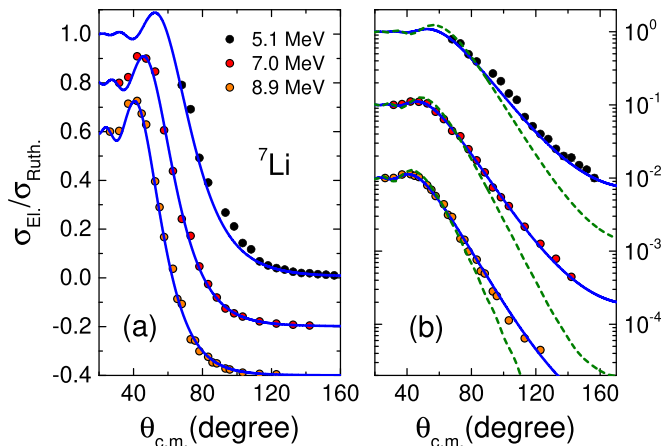


FIG. 8. The same as Fig. 5, for $^7\text{Li} + ^{120}\text{Sn}$. Data were extracted from Refs. [19,29].

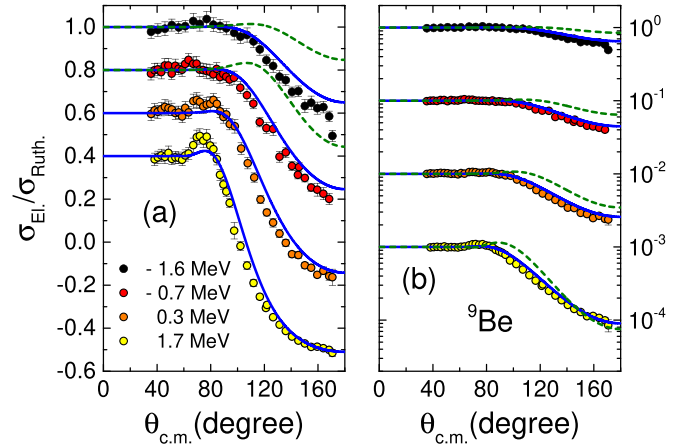


FIG. 9. The same as Fig. 5, for $^9\text{Be} + ^{120}\text{Sn}$. Data were extracted from Ref. [11].

Eq. (4) with two adjustable parameters, N_R and N_I , in order to fit the data more accurately, and compare the behavior of the corresponding OP parameter values obtained for different projectiles.

A. Uncertainties of the N_R and N_I values

In this section, we discuss some ambiguity inherent to the extraction of the N_R and N_I best fit values and their respective uncertainties. For this purpose, we have performed several calculations in order to verify the sensitivity of the data fit on variations of the N_R and N_I parameter values. Just as an example, we illustrate here the results obtained with the data set for ^{18}O at $E_{\text{Red}} = 2.1$ MeV. The corresponding best data fit is obtained with $N_R = 0.739$ and $N_I = 0.877$, with reduced χ square of $\chi^2 = 5.80$.

In Fig. 12(a), we present the values of χ^2 as a function of N_I for several (fixed) values of N_R . For each N_R , there is an optimum N_I value that provides the smallest χ^2 . Here, we can observe the strong correlation between the N_R and N_I parameters. This correlation can be even better observed in

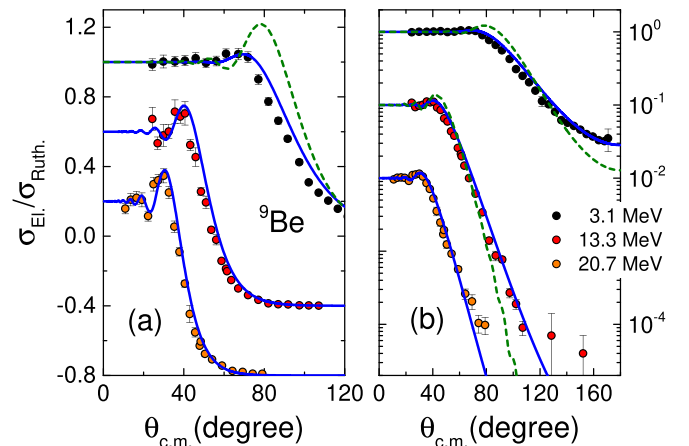


FIG. 10. The same as Fig. 5, for $^9\text{Be} + ^{120}\text{Sn}$. Data were extracted from Ref. [11].

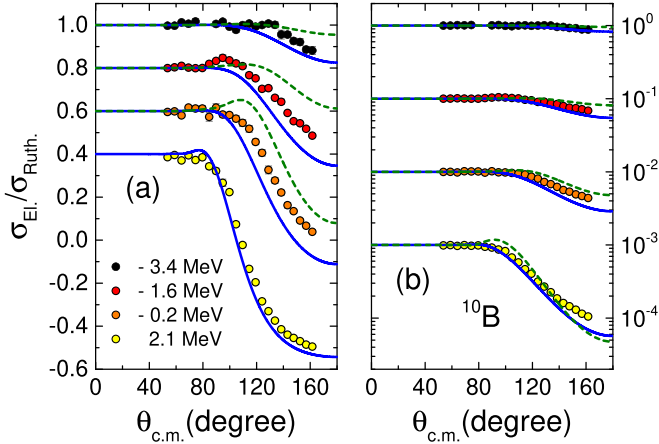


FIG. 11. The same as Fig. 5, for $^{10}\text{B} + ^{120}\text{Sn}$. Data were extracted from Refs. [12,20].

Fig. 12(b), which presents the optimum N_I value as a function of N_R . Clearly, for larger N_R values we have smaller values of optimum N_I . In Fig. 12(d), we show the χ^2 (obtained with the optimum N_I) as a function of N_R . In Fig. 12(c), we show three curves (in the N_R - N_I plane) that correspond to different levels of χ^2 (and also the point that provides the best $\chi^2 = 5.80$ for this data set).

Within the context of the theory of errors, the uncertainty of an adjustable parameter can be approximately estimated considering variations of the reduced χ square by about $1/N$ around the minimum χ^2 value (which should be close to 1), where N is the number of data. The experimental angular distribution, adopted as an example, contains 18 data points, and therefore $1/N \approx 0.06$. Since the best $\chi^2 = 5.80$, one should consider the range $\chi^2 \leq 5.86$ for the determination of the error bars of the parameters. Nevertheless, the OM is only

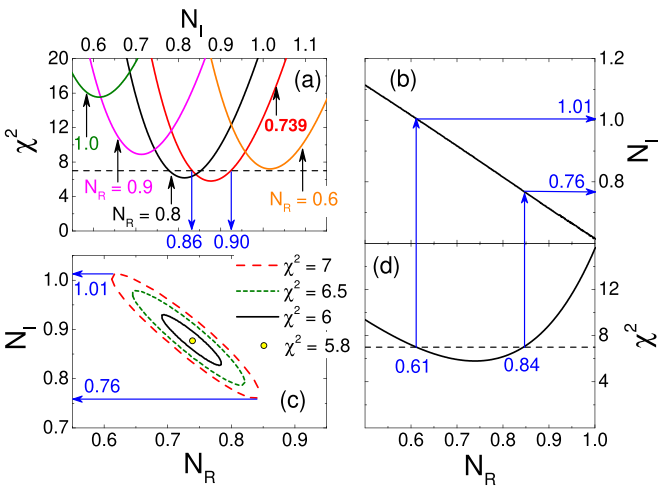


FIG. 12. The figure shows results obtained by fitting an experimental angular distribution for ^{18}O at $E_{\text{Red}} = 2.1$ MeV. (a) χ^2 versus N_I for some N_R values. (b) Optimum N_I value as a function of N_R . (c) Curves in the plane N_R - N_I that correspond to some levels of χ^2 . (d) χ^2 obtained with the optimum N_I as a function of N_R . See text for details.

a simple (in fact simplified) theoretical model to describe the experimental phenomenon, and one can not expect the theory of errors to work perfectly in this case. For instance, the best $\chi^2 = 5.80$ is very far from the expected value $\chi^2 \approx 1$ of the theory.

Taking into account this point, in many works, the estimate of uncertainties of the OM adjustable parameters is performed considering a different level of reduced χ square, for instance, an increase of 10% or 20% relative to its minimum value. Nevertheless, oftentimes the correlation between the parameters (as that for N_R with N_I) is not considered when determining uncertainties. In this case, the uncertainties can be largely underestimated.

Just to illustrate this point, let us suppose that we choose the level $\chi^2 = 7$ (about 20% above the best $\chi^2 = 5.80$) to determine the uncertainties. This level is represented by the dashed line in Fig. 12(a). The solid red curve in this figure corresponds to the variation of χ^2 as a function of N_I for the fixed (and also the best fit value) $N_R = 0.739$. If one neglects the N_R - N_I correlation, the uncertainty of the N_I parameter is found according to the intersections of the solid red curve with the $\chi^2 = 7$ level (dashed line). The blue arrows in Fig. 12(a) show the corresponding region of uncertainty: $0.86 \leq N_I \leq 0.90$ (relative uncertainty of about 4.5%). However, an inspection of the curve corresponding to the $\chi^2 = 7$ level in Fig. 12(c) shows that, when considering the N_R - N_I correlation, a better estimate for the uncertainty of N_I is $0.76 \leq N_I \leq 1.01$, therefore a much larger range of about 28% for the relative uncertainty. The same could be said about the N_R uncertainty. The dashed line in Fig. 12(d) also represents the level $\chi^2 = 7$. The corresponding N_R region is $0.61 \leq N_R \leq 0.84$ (about 32% of relative uncertainty in N_R). This region already contains the effect of the correlation [since the χ^2 versus N_R curve of Fig. 12(b) was obtained considering the variation of the optimum N_I value with N_R]. The blue arrows that connect Figs. 12(b) and 12(d) illustrate the effect of the correlation on the uncertainties of the N_R and N_I parameter values. In our example, the consideration or not of the correlation affects the parameter uncertainty values by a factor about 6.

Another important question can be raised here. What would be a good χ^2 level to estimate uncertainties? In our example, we chose 20% above the best (minimum) χ^2 . The best χ^2 is obtained with $N_R = 0.739$ and $N_I = 0.877$, while the borders ($\chi^2 = 7$) correspond to two possible pairs: $N_R = 0.61$ and $N_I = 1.01$ or $N_R = 0.84$ and $N_I = 0.76$. In Fig. 13 we present, in linear [Fig. 13(a)] and logarithmic [Fig. 13(b)] scales, the experimental angular distribution for ^{18}O at $E_{\text{Red}} = 2.1$ MeV, and three theoretical curves. Two of them, the solid black and dashed red lines, correspond to the best $\chi^2 = 5.80$ and to one case where $\chi^2 = 7$. These two lines are almost indistinguishable, indicating that this increase of 20% in χ^2 is probably too small to represent actual significance. The other curve (dotted blue lines in the figure) represents the result of a fit, in which $N_R = 1$ was fixed and only N_I was considered as an adjustable parameter. The corresponding optimum $N_I = 0.616$ was found, with $\chi^2 = 15.54$. Despite the difference of a factor of about 3 between the respective χ^2 values, both OPs (of the best $\chi^2 = 5.80$ and that with $\chi^2 = 15.54$) provide

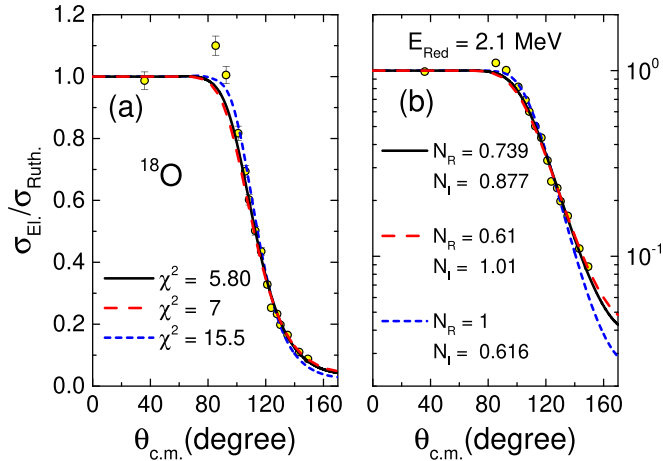


FIG. 13. Experimental angular distribution for ^{18}O at $E_{\text{Red}} = 2.1$ MeV, in linear (a) and logarithmic (b) scales. The solid black lines represent the best data fit ($\chi^2 = 5.80$) obtained within the OM. The dashed red lines were obtained with $N_R = 0.61$ and $N_I = 1.01$ that provide $\chi^2 = 7$. The dotted blue lines correspond to the result of the fit in which $N_R = 1$ was fixed and only the N_I value was adjusted ($\chi^2 = 15.54$).

quite reasonable data fits (see the black and blue lines in Fig. 13). The large difference between the respective χ^2 is mostly related to the fit in the backward angular region (in particular for the datum at the last angle $\theta_{\text{c.m.}} \approx 150^\circ$). On the other hand, the fit with $\chi^2 = 15.54$ (dotted blue lines in the figure) clearly provides a slightly better data description in the rainbow region ($\theta_{\text{c.m.}} \approx 90^\circ$). Thus, one might ask: taking into account the physical behavior, does the fit with $\chi^2 = 5.80$ actually describe the experimental data in a better way than that with $\chi^2 = 15.54$?

Thus, uncertainties of adjustable parameter values obtained from OM data fits should be considered just as rough estimates. If the strong correlation between N_R and N_I is taken into account (and it should be), the uncertainties of these parameters become quite large. In addition, as commented in the previous paragraph, it is possible to obtain a quite reasonable description of the experimental angular distribution (^{18}O at $E_{\text{Red}} = 2.1$ MeV) assuming very different N_R values. The reason for this behavior is also related to the correlation between the N_R and N_I parameters. As illustrated in Fig. 13, the (best fit) pair $N_R = 0.739$ and $N_I = 0.877$ produces OM cross sections similar to those obtained with (fixed) $N_R = 1$ and (adjusted) $N_I = 0.616$ (despite the large difference of a factor of 3 in the corresponding χ^2 values).

This behavior observed for the angular distribution of ^{18}O at $E_{\text{Red}} = 2.1$ MeV is also present in many other cases (projectiles and energies). The correlation between N_R and N_I implies a wide ambiguity in the determination of these parameter values, when simultaneously adjusted within the context of the OM data fits. In principle, the effect of the polarization due to inelastic channels would affect both: the real and imaginary parts of the OP. Even so, in order to avoid this question of correlation and consequent ambiguity, from now on we assume $N_R = 1$ in the OM calculations, and adjust only the N_I parameter value in the data fits.

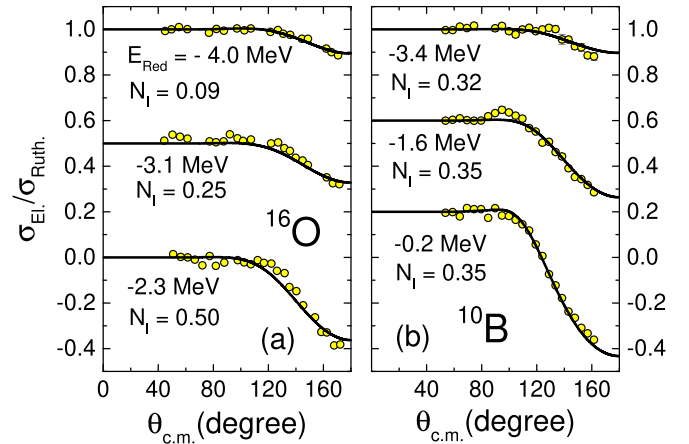


FIG. 14. Experimental angular distributions for ^{16}O and ^{10}B and corresponding theoretical OM cross sections obtained from data fits. The reduced energies and N_I values are indicated in the figure.

B. Sub-barrier region

When comparing data for different systems, it is important to take into account the region of energy considered. Thus, in this section we compare N_I values obtained for different projectiles in approximately the same region of reduced energy.

As illustrated in Figs. 3(a) and 11, at energies below the barrier, both systems, with ^{16}O and ^{10}B , present data with behavior in between the theoretical results of OIA (internal absorption = weak surface absorption) and SSA (strong surface absorption). In Fig. 14, we present the results obtained through OM data fits, for ^{16}O [Fig. 14(a)] and ^{10}B [Fig. 14(b)]. The figure also shows the N_I values obtained for each angular distribution. The ^{16}O case presents the expected behavior of strongly bound nuclei: vanishing surface absorption at 4 MeV below the barrier ($N_I = 0.09$), and increasing $N_I = 0.25$ and 0.50 values when approaching the barrier. On the other hand, the N_I values for ^{10}B are quite similar (about 0.35) for the three energies below the barrier, indicating that the surface absorption does not decrease significantly even at sub-barrier energies.

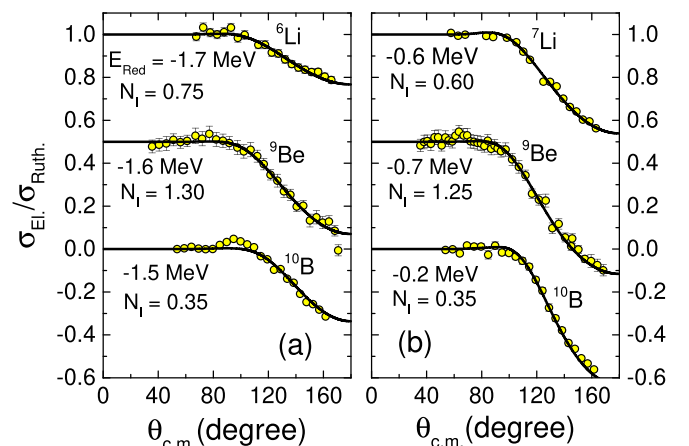


FIG. 15. The same as Fig. 14, for other systems and energies.

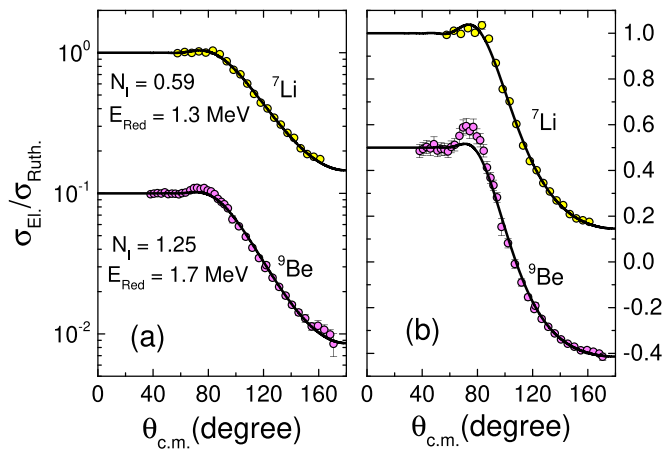


FIG. 16. Experimental angular distributions for ${}^7\text{Li}$ and ${}^9\text{Be}$, in (a) logarithmic and (b) linear scales. The black lines represent the OM fits (performed by adjusting only the N_I parameter). The corresponding N_I and reduced energy values are indicated in the figure.

In Fig. 15(a), we present results for the weakly bound ${}^6\text{Li}$, ${}^9\text{Be}$, and ${}^{10}\text{B}$ projectiles, at energies about 1.6 MeV below the barrier. In Fig. 15(b), we have ${}^7\text{Li}$ (instead ${}^6\text{Li}$) and again ${}^9\text{Be}$ and ${}^{10}\text{B}$, at energies about 0.5 MeV below the barrier. Even in this low-energy region, the three projectiles present nonvanishing N_I values, the largest being those for ${}^9\text{Be}$ ($N_I \approx 1.3$), followed by those for the lithium isotopes (about 0.7), and the small one (0.35) being that for ${}^{10}\text{B}$. This behavior indicates more absorption at sub-barrier energies, probably due to the breakup process, for ${}^6,7\text{Li}$ and ${}^9\text{Be}$ [2,11].

C. Above-barrier region

Now we analyze angular distributions at energies above the barrier. Again we present comparison of data only in similar reduced energy regions. For a good appreciation of the results, the figures contain both linear and logarithmic scales.

Figure 16 presents angular distributions for ${}^7\text{Li}$ and ${}^9\text{Be}$ at $E_{\text{Red}} \approx 1.5$ MeV. The N_I values of about 0.6 for ${}^7\text{Li}$ and 1.2 for

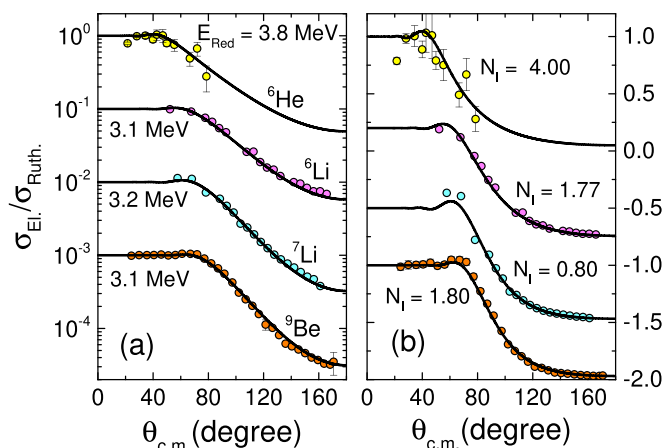


FIG. 17. The same of Fig. 16, for other projectiles and energies.

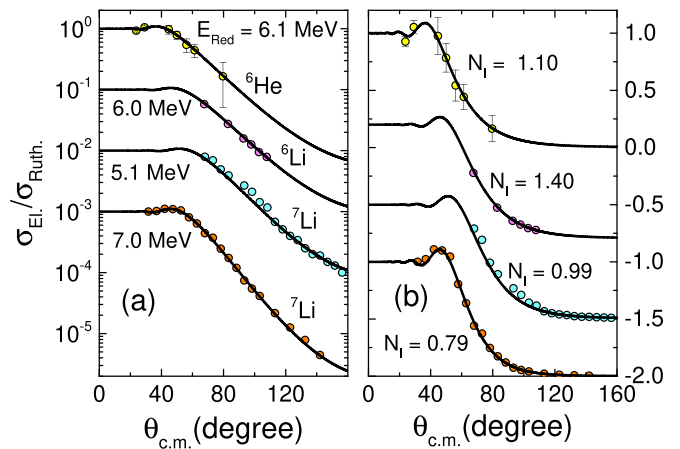


FIG. 18. The same of Fig. 16, for other projectiles and energies.

${}^9\text{Be}$ are quite similar to those obtained at sub-barrier energies (see Fig. 15).

Figure 17 presents results for ${}^6\text{He}$, ${}^6\text{Li}$, ${}^7\text{Li}$, and ${}^9\text{Be}$ at about 3.5 MeV above the barrier. The best fit $N_I = 4$ obtained for ${}^6\text{He}$ is a very large value. However, we point out that, due to the large error bars of the cross section data, the sensitivity of the χ^2 to the N_I parameter value is very weak for this angular distribution, and much smaller N_I values also provide a good data fit. The N_I values obtained for the weakly bound ${}^6\text{Li}$, ${}^7\text{Li}$, and ${}^9\text{Be}$ nuclei are large, again indicating strong surface absorption in these cases.

Figure 18 presents results for ${}^6\text{He}$, ${}^6\text{Li}$, and ${}^7\text{Li}$ (two energies) at $E_{\text{Red}} \approx 6$ MeV. The ${}^6\text{He}$ and ${}^6\text{Li}$ OM fits result in N_I values larger than 1. The two energies for ${}^7\text{Li}$ provide, consistently, similar values around $N_I \approx 0.89$.

Finally, Fig. 19 presents results for the strongly bound ${}^4\text{He}$ and the weakly bound ${}^9\text{Be}$ nuclei, at very high energies $E_{\text{Red}} \approx 20$ MeV. A striking difference of about one order of magnitude is observed for the corresponding N_I values: 0.20 and 1.90.

In Fig. 20, we show the N_I values as a function of the reduced energy for several projectiles. We have not included

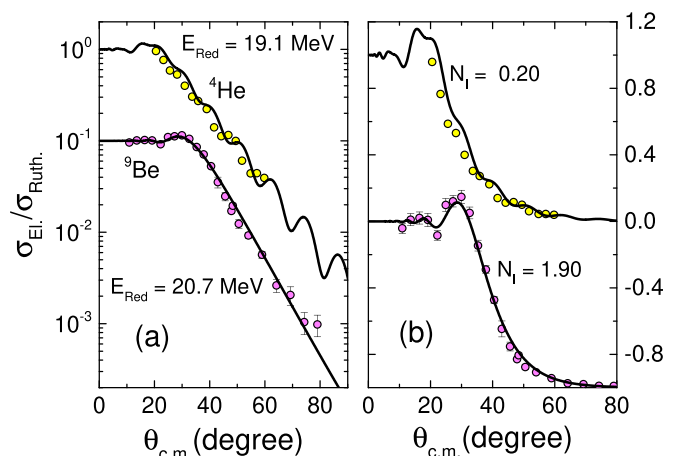


FIG. 19. The same of Fig. 16, for other projectiles and energies.

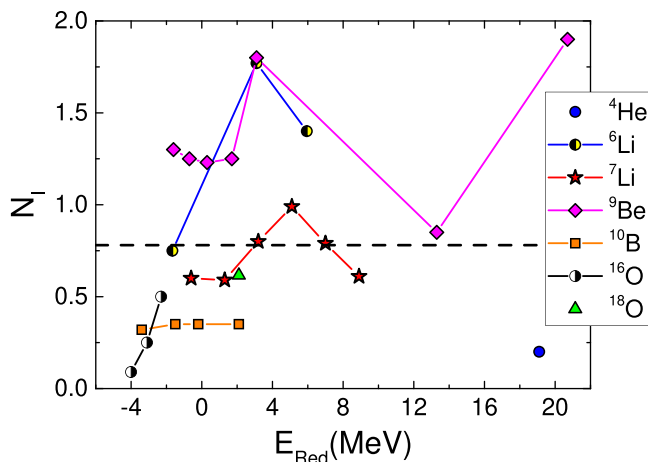


FIG. 20. N_I values obtained from OM data analyses as a function of the reduced energy for several projectiles. The solid lines in the figure are only guides for the eye, while the dashed line corresponds to the standard $N_I = 0.78$.

the results for ${}^6\text{He}$ and ${}^4\text{He}$, at low energies, because the χ^2 for these distributions are not very sensitive to the N_I values, due to the large error bars of the experimental cross sections. The solid lines in this figure are only guides for the eye. The dashed line corresponds to the standard $N_I = 0.78$ value. Considering only the behavior of the weakly bound nuclei, the figure indicates increasing N_I parameter values in the following order: ${}^{10}\text{B}$, ${}^7\text{Li}$, ${}^6\text{Li}$, and ${}^9\text{Be}$.

VI. CONCLUSIONS

In this paper, we have presented new data for the elastic scattering of ${}^6\text{Li} + {}^{120}\text{Sn}$ at $E_{\text{LAB}} = 19, 24,$ and 27 MeV. The corresponding angular distributions were considered together with other elastic scattering data of several projectiles on the same target nucleus. The complete data set was systematically analyzed within the context of the OM. We have demonstrated that the SPP in the context of the standard SSA provides a quite reasonable description of the data for all systems, without the necessity of any adjustable parameter. We have obtained more accurate agreement between data and theoretical cross sections by considering adjustable OP strengths in order to improve the data fits.

We have illustrated the strong correlation between the real and imaginary adjustable strength factors (N_R and N_I) in an

example with one angular distribution. If this correlation is taken into account, the uncertainties of the N_R and N_I best fit values become very large. In addition, different pairs of these parameters, with corresponding χ^2 values that differ by a factor as large as 3, provide rather similar theoretical angular distributions that agree well with the data. This behavior is also found for other projectiles and energies. In order to avoid this ambiguity, we have assumed the SPP for the real part of the OP, with fixed standard $N_R = 1$, and adjusted only the N_I parameter value in the OM data fits.

As observed in Figs. 14–19, the theoretical cross sections obtained through OM fits with only one free parameter (N_I) are in quite good agreement with the data for all systems and energies. We have studied the behavior of the best fit N_I value in different energy regions, and compared results obtained for the various projectiles. The weakly bound ${}^{6,7}\text{Li}$, ${}^9\text{Be}$, and ${}^{10}\text{B}$ projectiles present significant N_I values at sub-barrier energies, indicating strong surface absorption even in this low-energy region, a characteristic probably related to the breakup process. Still considering these nuclei, increasing N_I parameter values are observed in the following order: ${}^{10}\text{B}$, ${}^7\text{Li}$, ${}^6\text{Li}$, and ${}^9\text{Be}$. This order is related to the binding energy of these nuclei (presented as Q values in Table I). This suggests a clear correlation between the breakup probability and the absorption of flux from the elastic channel.

ACKNOWLEDGMENTS

This work was supported by the Ministry of Science, Innovation and Universities of Spain, through the project PGC2018-096994-B-C21. This work was also partially supported by the Spanish Ministry of Economy and Competitiveness, the European Regional Development Fund (FEDER), under Project No. FIS2017-88410-P and by the European Union's Horizon 2020 research and innovation program, under Grant Agreement No. 654002. This work has also been partially supported by Fundação de Amparo à Pesquisa do Estado de São Paulo (FAPESP) Proc. No. 2018/09998-8 and No. 2017/05660-0, Conselho Nacional de Desenvolvimento Científico e Tecnológico (CNPq) Proc. No. 407096/2017-5 and No. 306433/2017-6, and, finally, it is a part of the project INCT-FNA Proc. No. 464898/2014-5. A.A. acknowledges Grant No. PIP00786CO from CONICET. D.A.T. and F.R. acknowledge support from Colciencias under contract 110165842984.

- [1] H. Horiuchi, *J. Phys.: Conf. Ser.* **436**, 012003 (2013).
- [2] D. H. Luong, M. Dasgupta, D. J. Hinde, R. du Rietz, R. Rafiei, C. J. Lin, M. Evers, and A. Díaz-Torres, *Phys. Rev. C* **88**, 034609 (2013).
- [3] D. Escrig, A. Sánchez-Benítez, A. Moro, M. A. G. Alvarez, M. Andrés, C. Angulo, M. Borge, J. Cabrera, S. Cherubini, P. Demaret, J. Espino, P. Figuera, M. Freer, J. García-Ramos, J. Gómez-Camacho, M. Gulino, O. Kakuee, I. Martel, C. Metelko, F. Pérez-Bernal, J. Rahighi, K. Rusek, D. Smirnov, O. Tengblad, and V. Ziman, *Nucl. Phys. A* **792**, 2 (2007).

- [4] A. Di Pietro, P. Figuera, F. Amorini, C. Angulo, G. Cardella, S. Cherubini, T. Davinson, D. Leanza, J. Lu, H. Mahmud, M. Milin, A. Musumarra, A. Ninane, M. Papa, M. G. Pellegriti, R. Raabe, F. Rizzo, C. Ruiz, A. C. Shotton, N. Soić, S. Tudisco, and L. Weissman, *Phys. Rev. C* **69**, 044613 (2004).
- [5] J. P. Fernández-García, M. Cubero, M. Rodríguez-Gallardo, L. Acosta, M. Alcorta, M. A. G. Alvarez, M. J. G. Borge, L. Buchmann, C. A. Diget, H. A. Falou, B. R. Fulton, H. O. U. Fynbo, D. Galaviz, J. Gómez-Camacho, R. Kanungo, J. A. Lay, M. Madurga, I. Martel, A. M. Moro, I. Mukha, T. Nilsson, A. M.

- Sánchez-Benítez, A. Shotter, O. Tengblad, and P. Walden, *Phys. Rev. Lett.* **110**, 142701 (2013).
- [6] D. R. Tilley, C. M. Cheves, J. L. Godwin, G. M. Hale, H. M. Hofmann, J. H. Kelley, C. G. Sheu, and H. R. Weller, *Nucl. Phys. A* **708**, 3 (2002).
- [7] M. Chaussidon, F. Robert, and K. D. McKeegan, *Geochim. Cosmochim. Acta* **70**, 224 (2006).
- [8] K. Lodders, *Astrophys. J.* **591**, 1220 (2003).
- [9] R. Ost, E. Speth, K. O. Pfeiffer, and K. Bethge, *Phys. Rev. C* **5**, 1835 (1972).
- [10] J. Casal, M. Rodríguez-Gallardo, J. M. Arias, and I. J. Thompson, *Phys. Rev. C* **90**, 044304 (2014).
- [11] A. Arazi, J. Casal, M. Rodríguez-Gallardo, J. M. Arias, R. Lichtenthäler Filho, D. Abriola, O. A. Capurro, M. A. Cardona, P. F. F. Carnelli, E. de Barbará, J. Fernández Niello, J. M. Figueira, L. Fimiani, D. Hojman, G. V. Martí, D. Martínez Heimman, and A. J. Pacheco, *Phys. Rev. C* **97**, 044609 (2018).
- [12] M. A. G. Alvarez, M. Rodríguez-Gallardo, L. R. Gasques, L. C. Chamon, J. R. B. Oliveira, V. Scarduelli, A. S. Freitas, E. S. Rossi, V. A. B. Zagatto, J. Rangel, J. Lubian, and I. Padron, *Phys. Rev. C* **98**, 024621 (2018).
- [13] A. M. Sánchez-Benítez, D. Escrig, M. A. G. Alvarez, M. V. Andrés, C. Angulo, M. J. G. Borge, J. Cabrera, S. Cherubini, P. Demaret, J. M. Espino, P. Figuera, M. Freer, J. García-Ramos, J. Gómez-Camacho, M. Gulino, O. Kakuee, I. Martel, C. Metelko, A. Moro, F. Pérez-Bernal, J. Rahighi, K. Rusek, D. Smirnov, O. Tengblad, P. V. Duppen, and V. Ziman, *Nucl. Phys. A* **803**, 30 (2008).
- [14] L. Acosta *et al.*, *Eur. Phys. J. A* **42**, 461 (2009).
- [15] L. Acosta, A. M. Sánchez-Benítez, M. E. Gómez, I. Martel, F. Pérez-Bernal, F. Pizarro, J. Rodríguez-Quintero, K. Rusek, M. A. G. Alvarez, M. V. Andrés, J. M. Espino, J. P. Fernández-García, J. Gómez-Camacho, A. M. Moro, C. Angulo, J. Cabrera, E. Casarejos, P. Demaret, M. J. G. Borge, D. Escrig, O. Tengblad, S. Cherubini, P. Figuera, M. Gulino, M. Freer, C. Metelko, V. Ziman, R. Raabe, I. Mukha, D. Smirnov, O. R. Kakuee, and J. Rahighi, *Phys. Rev. C* **84**, 044604 (2011).
- [16] R. Rafiei, R. du Rietz, D. H. Luong, D. J. Hinde, M. Dasgupta, M. Evers, and A. Díaz-Torres, *Phys. Rev. C* **81**, 024601 (2010).
- [17] D. H. Luong, M. Dasgupta, D. Hinde, R. du Rietz, R. Rafiei, C. Lin, M. Evers, and A. Díaz-Torres, *Phys. Lett. B* **695**, 105 (2011).
- [18] S. Kalkal, E. C. Simpson, D. H. Luong, K. J. Cook, M. Dasgupta, D. J. Hinde, I. P. Carter, D. Y. Jeung, G. Mohanto, C. S. Palshetkar, E. Prasad, D. C. Rafferty, C. Simenel, K. Vo-Phuoc, E. Williams, L. R. Gasques, P. R. S. Gomes, and R. Linares, *Phys. Rev. C* **93**, 044605 (2016).
- [19] V. A. B. Zagatto, J. Lubian, L. R. Gasques, M. A. G. Alvarez, L. C. Chamon, J. R. B. Oliveira, J. A. Alcántara-Núñez, N. H. Medina, V. Scarduelli, A. Freitas, I. Padron, E. S. Rossi, and J. M. B. Shorto, *Phys. Rev. C* **95**, 064614 (2017).
- [20] L. R. Gasques, A. S. Freitas, L. C. Chamon, J. R. B. Oliveira, N. H. Medina, V. Scarduelli, E. S. Rossi, M. A. G. Alvarez, V. A. B. Zagatto, J. Lubian, G. P. A. Nobre, I. Padron, and B. V. Carlson, *Phys. Rev. C* **97**, 034629 (2018).
- [21] L. C. Chamon, B. V. Carlson, L. R. Gasques, D. Pereira, C. De Conti, M. A. G. Alvarez, M. S. Hussein, M. A. Cândido Ribeiro, E. S. Rossi, and C. P. Silva, *Phys. Rev. C* **66**, 014610 (2002).
- [22] P. Mohr, P. N. de Faria, R. Lichtenthäler, K. C. C. Pires, V. Guimarães, A. Lépine-Szily, D. R. Mendes, A. Arazi, A. Barioni, V. Morcelle, and M. C. Morais, *Phys. Rev. C* **82**, 044606 (2010).
- [23] I. Kumabe, H. Ogata, T.-H. Kim, M. Inoue, Y. Okuma, and M. Matoba, *J. Phys. Soc. Jpn.* **25**, 14 (1968).
- [24] C. Silva, M. Alvarez, L. Chamon, D. Pereira, M. Rao, E. R. Jr., L. Gasques, M. Santo, R. Anjos, J. Lubian, P. Gomes, C. Muri, B. Carlson, S. Kailas, A. Chatterjee, P. Singh, A. Shrivastava, K. Mahata, and S. Santra, *Nucl. Phys. A* **679**, 287 (2001).
- [25] H. G. Bohlen, K. D. Hildenbrand, A. Gobbi, and K. I. Kubo, *Z. Phys. A: At. Nucl.* **273**, 211 (1975).
- [26] P. N. de Faria, R. Lichtenthäler, K. C. C. Pires, A. M. Moro, A. Lépine-Szily, V. Guimarães, D. R. J. Mendes, A. Arazi, M. Rodríguez-Gallardo, A. Barioni, V. Morcelle, M. C. Morais, O. Camargo, J. Alcántara Nuñez, and M. Assunção, *Phys. Rev. C* **81**, 044605 (2010).
- [27] S. Appannababu, R. Lichtenthäler, M. A. G. Alvarez, M. Rodríguez-Gallardo, A. Lépine-Szily, K. C. C. Pires, O. C. B. Santos, U. U. Silva, P. N. de Faria, V. Guimarães, E. O. N. Zevallos, V. Scarduelli, M. Assunção, J. M. B. Shorto, A. Barioni, J. Alcántara-Nuñez, and V. Morcelle., *Phys. Rev. C* **99**, 014601 (2019).
- [28] K. Zerva *et al.*, *Eur. Phys. J. A* **48**, 102 (2012).
- [29] A. Kundu, S. Santra, A. Pal, D. Chattopadhyay, R. Tripathi, B. J. Roy, T. N. Nag, B. K. Nayak, A. Saxena, and S. Kailas, *Phys. Rev. C* **95**, 034615 (2017).
- [30] G. R. Satchler and W. G. Love, *Phys. Rep.* **55**, 183 (1979).
- [31] G. R. Satchler, *Direct Nuclear Reactions* (Clarendon Press, Oxford, 1983).
- [32] G. R. Satchler, *Phys. Rep.* **199**, 147 (1991).
- [33] G. R. Satchler, M. A. Nagarajan, J. S. Lilley, and I. J. Thompson, *Ann. Phys. (NY)* **178**, 110 (1987).
- [34] D. T. Khoa, *Nucl. Phys. A* **484**, 376 (1988).
- [35] M. E. Brandan and G. R. Satchler, *Nucl. Phys. A* **487**, 477 (1988).
- [36] S. M. Lenzi, A. Vitturi, and F. Zardi, *Phys. Rev. C* **40**, 2114 (1989).
- [37] G. R. Satchler, *Nucl. Phys. A* **579**, 241 (1994).
- [38] M. E. Brandan and G. R. Satchler, *Phys. Rep.* **285**, 143 (1997).
- [39] G. Pollarolo, R. A. Broglia, and A. Winther, *Nucl. Phys. A* **361**, 307 (1981).
- [40] G. Pollarolo, R. A. Broglia, and A. Winther, *Nucl. Phys. A* **406**, 369 (1983).
- [41] Y. Sakuragi, *Phys. Rev. C* **35**, 2161 (1987).
- [42] M. A. G. Alvarez, L. C. Chamon, M. S. Hussein, D. Pereira, L. R. Gasques, E. S. Rossi, and C. P. Silva, *Nucl. Phys. A* **723**, 93 (2003).
- [43] D. Pereira, E. S. Rossi, Jr., G. P. A. Nobre, L. C. Chamon, C. P. Silva, L. R. Gasques, M. A. G. Alvarez, R. V. Ribas, J. R. B. Oliveira, N. H. Medina, M. N. Rao, E. W. Cybulska, W. A. Seale, N. Carlin, P. R. S. Gomes, J. Lubian, and R. M. Anjos, *Phys. Rev. C* **74**, 034608 (2006).
- [44] J. P. Fernández-García, M. Rodríguez-Gallardo, M. A. G. Alvarez, and A. M. Moro, *Nucl. Phys. A* **840**, 19 (2010).
- [45] J. P. Fernández-García, M. A. G. Alvarez, and L. C. Chamon, *Phys. Rev. C* **92**, 014604 (2015).
- [46] L. R. Gasques, L. C. Chamon, D. Pereira, M. A. G. Alvarez, E. S. Rossi, C. P. Silva, and B. V. Carlson, *Phys. Rev. C* **69**, 034603 (2004).
- [47] L. Canto, P. Gomes, J. Lubian, L. Chamon, and E. Crema, *Nucl. Phys. A* **821**, 51 (2009).

- [48] G. P. A. Nobre, C. P. Silva, L. C. Chamon, and B. V. Carlson, *Phys. Rev. C* **76**, 024605 (2007).
- [49] G. Nobre, L. Chamon, B. Carlson, I. Thompson, and L. Gasques, *Nucl. Phys. A* **786**, 90 (2007).
- [50] G. P. A. Nobre, L. C. Chamon, L. R. Gasques, B. V. Carlson, and I. J. Thompson, *Phys. Rev. C* **75**, 044606 (2007).
- [51] H. Feshbach, *Theoretical Nuclear Physics* (Wiley, New York, 1992).
- [52] B. V. Carlson and D. Hirata, *Phys. Rev. C* **62**, 054310 (2000).
- [53] G. A. Lalazissis, J. König, and P. Ring, *Phys. Rev. C* **55**, 540 (1997).
- [54] T. Nikšić, D. Vretenar, P. Finelli, and P. Ring, *Phys. Rev. C* **66**, 024306 (2002).
- [55] G. D. Alkhazov, M. N. Andronenko, A. V. Dobrovolsky, P. Egelhof, G. E. Gavrilov, H. Geissel, H. Irnich, A. V. Khanzadeev, G. A. Korolev, A. A. Lobodenko, G. Münzenberg, M. Mutterer, S. R. Neumaier, F. Nickel, W. Schwab, D. M. Seliverstov, T. Suzuki, J. P. Theobald, N. A. Timofeev, A. A. Vorobyov, and V. I. Yatsoura, *Phys. Rev. Lett.* **78**, 2313 (1997).